Supplemental Information

Elucidating the mechanisms of MgB_2 hydrogenation via a combined experiment-theory study

K.G. Ray[1], L.E. Klebanoff*[2], J.R.I. Lee[1], V. Stavila[2], T.W. Heo[1], P. Shea[1], A.A. Baker[1], S. Kang[1], M. Bagge-Hansen[1], Y.-S. Liu[3], J.L. White[2], and B.C. Wood[1]

[1]Lawrence Livermore National Laboratory, Livermore CA 94551

[2]Sandia National Laboratories, Livermore CA 94551

[3]Lawrence Berkeley National Laboratory, Berkeley CA 94720

*Corresponding Author, E-mail: lekleba@sandia.gov

***Depth sensitivities*:** Research into the initial stages of hydrogenation in a material necessitates the use of a variety of methods that provide the capabilities for characterization of structure and bonding with distinct depth sensitivities. This study makes extensive use of Fourier Transform Infrared (FTIR) spectroscopy, x-ray diffraction (XRD), x-ray absorption spectroscopy (XAS), and soft x-ray emission spectroscopy (XES), that offer the ability to probe both surface and bulk phenomena in MgB_2. It is valuable, therefore, to discuss the relative depth sensitivities of the techniques.

XAS and XES have not been extensively used in the characterization of hydrogen storage materials but thorough discussions of both techniques can be found in the literature.[1] Two modes of detection, total electron yield (TEY) and total fluorescence yield (TFY),[1,2] were used in measurement of the XAS for this study and each offers a distinct depth sensitivity. Since the TEY corresponds to the secondary electron current from the sample, the depth probed by the TEY signal is governed by the mean free path of the original electrons generated during Auger decay of the x-ray photo-excited atom.

Figure S1 plots the contribution from a layer of atoms a distance X_o below the surface to the total secondary electron yield for B K-edge and Mg K-edge XAS-TEY for MgB_2 using the model of Erbil.[3]

For secondary electrons generated by Auger electrons originating from the B K-edge (i.e. B KLL Auger electrons), the vast majority of the secondary electron yield (and hence the XAS-TEY spectrum) comes from within ~50 Å (5 nm) of the surface. Such surface sensitivity arises due to the high inelastic scattering cross section for 172 eV B KLL

Auger electrons travelling through MgB_2. The TFY signal, which arises from fluorescence photons emitted during decay of x-ray photo-excited atoms, has greater depth sensitivity than the TEY signal because the photon attenuation length significantly exceeds the mean free path of the Auger electrons. An estimate of the depth sensitivity of B K-edge XAS-TFY measurements in this study can be obtained by considering the attenuation of B K_α photons (183.3 eV) in MgB_2 (attenuation length ~176 nm). At a photon energy of ~183 eV, ~95 % of the fluorescence photons would be emitted from within 175 nm of the sample surface at normal incidence.[4] Since the XES spectrum is obtained via energy resolved measurement of the fluorescence photons, this technique will have comparable depth sensitivity to the XAS-TFY. In contrast, for secondary electrons generated by Auger electrons originating from the Mg K-edge (Mg KLL Auger electrons), the entire secondary electron yield comes from within ~480 Å (48 nm) of the surface.[3] This is due to the relatively lower inelastic scattering cross section for 1173 eV Mg KLL Auger electrons travelling through MgB_2. For XAS-TFY measurements at the Mg K-edge, the depth of measurement is determined by the transmission of ~1250 – 1280 eV photons through MgB_2. For this photon energy range, ~ 95% of the light is emitted within 12100 nm of the sample surface.[4]

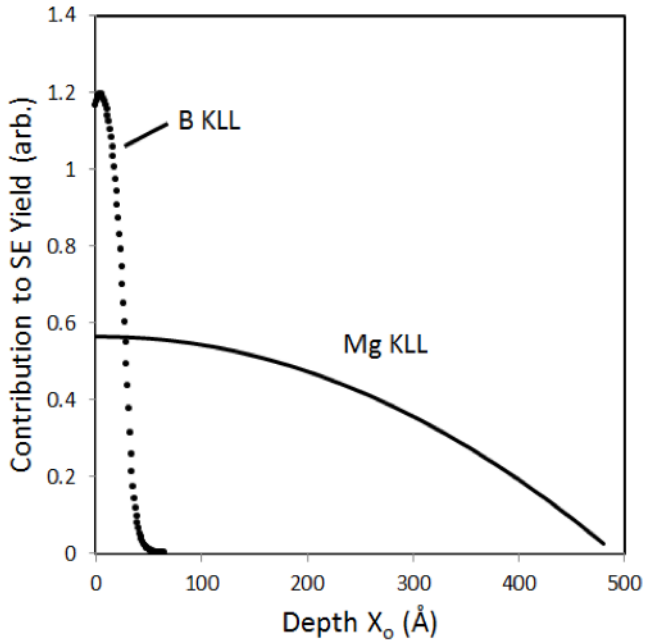

Figure S1: Contribution to the total secondary electron yield (TEY) from different layers of MgB_2 at depths X_o (Å) from the sample surface (at $X_o = 0$) for B K-edge (B KLL) and Mg K-edge (Mg KLL) XAS spectra. The calculations are based on the approach of Reference 3.

The remaining characterization techniques implemented in this study have greater bulk sensitivity than the soft x-ray XAS/XES. When FTIR measurements are conducted in the

attenuated total external reflectance (ATR) mode, the penetration depth of the evanescent IR wave into the material is 3,000 to 5,000 nm. Furthermore, the Cu K_α radiation ($h\nu$ = 8037 eV) used for the XRD measurements has an attenuation length in MgB_2 of ~ 264 µm.[4] Significantly, very little diffracted signal will be obtained from depths greater than one attenuation length (even at normal incidence), since the diffracted x-rays must transverse this distance twice: once into and once out of the sample. These depth sensitivities indicted above can be compared to other analytical methods typically employed for solid state hydrogen storage materials. The neutrons of energy ~35 meV used in neutron diffraction and ~20 – 25 meV used in neutron vibrational spectroscopy (NVS) have depth of penetrations of order micrometers if the material strongly absorbs neutrons like naturally occurring B with high concentrations of ^{10}B. For weakly neutron absorbing materials, such as those enriched in ^{11}B, the neutron penetration depth can increase to the centimeter range.[5] Meanwhile, the NMR measurements typically used in solid-state science have a depth of penetration of ~5 mm.

MgB_2 sample purity: Our initial attempts to use commercial MgB_2 revealed that the material possessed B impurities. This led to our in-house synthesis of MgB_2. The XRD spectrum shown in Figure S2 for this material shows an impurity-free MgB_2 XRD spectrum in good agreement with theoretical expectations.

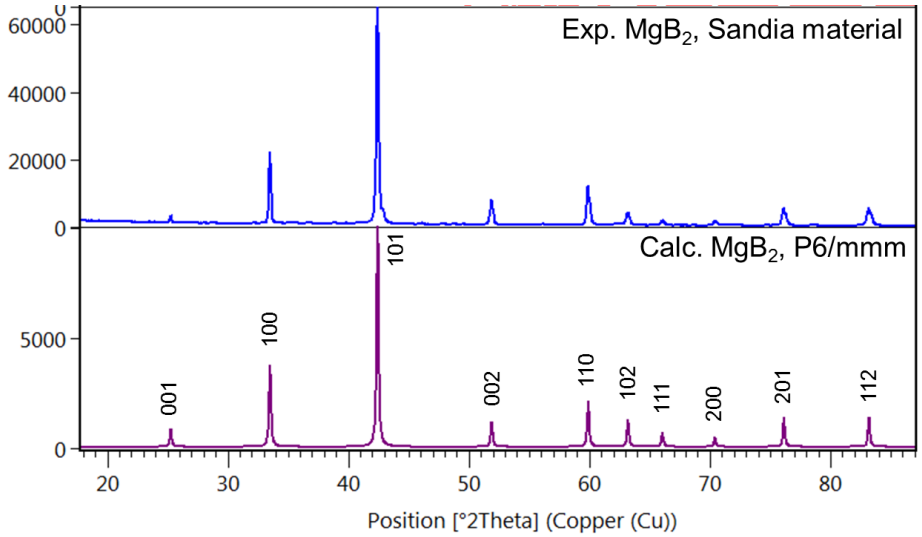

Figure S2: XRD patterns of MgB_2: (top) experimental XRD of MgB_2 synthesized at Sandia; (bottom) calculated MgB_2 XRD pattern shown for comparison.

Synthesis of $MgB_{12}H_{12}$*H_2O: Cesium dodecahydro-closo-dodecaborate, $Cs_2B_{12}H_{12}$, (466 mg, 1.0 mmol) was dissolved upon heating in 20 mL H_2O and the warm solution was passed through an Amberlite IR-120 ion-exchange column in H+ form. The acidic fraction was reacted with excess magnesium carbonate upon stirring at room temperature until pH=7 was achieved. The solvent was removed on a rotary evaporator to yield a

white powder. The monohydrate $MgB_{12}H_{12}$ salt was obtained upon heating. In a typical experiment, 250 mg of hydrated $MgB_{12}H_{12}$were loaded into a Schlenk tube and heated in vacuum as follows: (*i*) at 105 °C for 2 hours, then (*ii*) at 135 °C for 4 hours, and finally (*iii*) at 165 °C for 6 hrs. The isolated yield was ~79% based on initial $Cs_2B_{12}H_{12}$.

***Additional FTIR results*:** The FTIR spectrum of MgB_2 + 0.85 wt. % H in Figure 2(a) shows B-H bending peaks in good agreement with the known spectrum of $Mg(BH_4)_2$. However, there appears to be a shift of ~16 cm^{-1} towards lower wavenumbers for the MgB_2 + 0.85 wt. % H spectrum. Part of this may be due to its appearance on a more strongly sloped background. However, we wanted to understand the context of this shift, if it was large or small compared to the variations of $[BH_4]^-$ vibrational properties in other borohydride samples. Also, we investigated if the double-peaked nature of the FTIR peaks was unique to $Mg(BH_4)_2$.

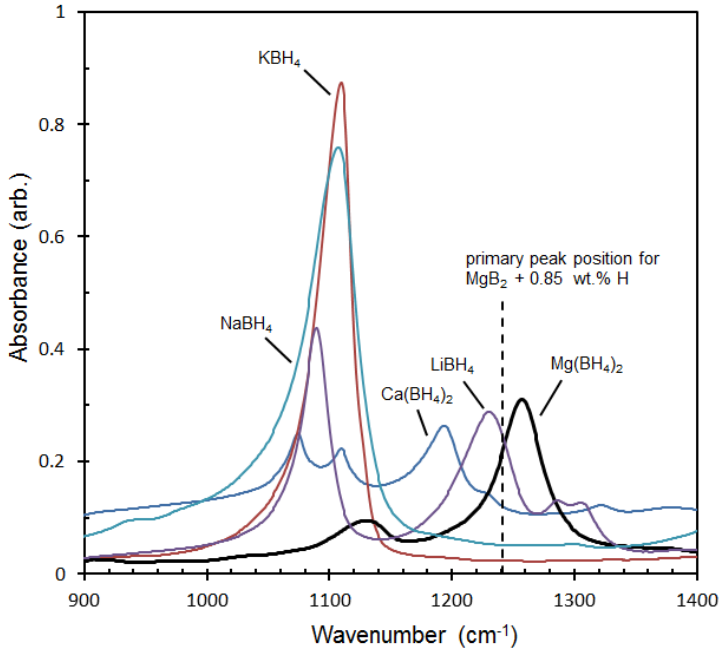

Figure S3: FTIR spectra in the 900 – 1400 cm^{-1} range for the representative borohydrides $Mg(BH_4)_2$, $Ca(BH_4)_2$, KBH_4, $LiBH_4$, $NaBH_4$.

Figure S3 plots the FTIR spectra in the wavenumber range of Figure 2(a) for a number of different borohydride materials with varying structures and counterions. There is seen a dramatic range of variability in the vibrational spectra, spanning a wavenumber range of ~ 157 cm^{-1}. In this context, a shift of 16 cm^{-1} between MgB_2 + 0.85 wt. % H and $Mg(BH_4)_2$ is not large, and the observed B-H peaks from MgB_2 + 0.85 wt. % H is closest in position and appearance to $Mg(BH_4)_2$. The FTIR of $Ca(BH_4)_2$ might be expected to be very similar to $Mg(BH_4)_2$ in vibrations and crystal structure. Yet, as shown in Figure S3,

there is a a 64 cm^{-1} shift in the main peak from just changing the counterion. By comparison a shift of 16 cm^{-1} is not large, and the difference between MgB_2 + 0.85 wt. % H and $Mg(BH_4)_2$ is a much smaller difference than changing the counterion. Figure S3 shows that the FTIR spectrum for MgB_2 + 0.85 wt. % H is in very close accord with that from $Mg(BH_4)_2$.

The FTIR spectrum of Figure 2(b) shows that there are no FTIR peaks from MgB_2 + 0.85 wt. % H in the wavenumber range where strong B-H stretches from intermediates are expected. Figure 2(b) utilizes FTIR data from a sample of $Na_2B_{10}H_{10}$ and NaB_3H_8 for comparison. Since these material have Na as the counterion, they may have FTIR spectra shifted far away from the Mg-analogues $Mg(B_3H_8)_2$ and $MgB_{10}H_{10}$ that would derive from the Mg in MgB_2. Unfortunately, samples of $Mg(B_3H_8)_2$ and $MgB_{10}H_{10}$ are unavailable, which necessitated the use of the Na analogues.

Figure S4 shows a comparison of FTIR data for the cage structure materials $MgB_{12}H_{12}$, $CaB_{12}H_{12}$, and $Na_2B_{12}H_{12}$ over the wavenumber range of Figure 2(b). The results show similar B-H stretch spectra in this wavenumber range even though the counterion is varying. This suggests that for related closoboroane materials like $MgB_{10}H_{10}$ and $Na_2B_{10}H_{10}$, there will also be little variation in the FTIR spectrum, justifying use in Figure 2(b) of $Na_2B_{10}H_{10}$ as a possible surrogate for $MgB_{10}H_{10}$ formation in the Mg-based MgB_2 system.

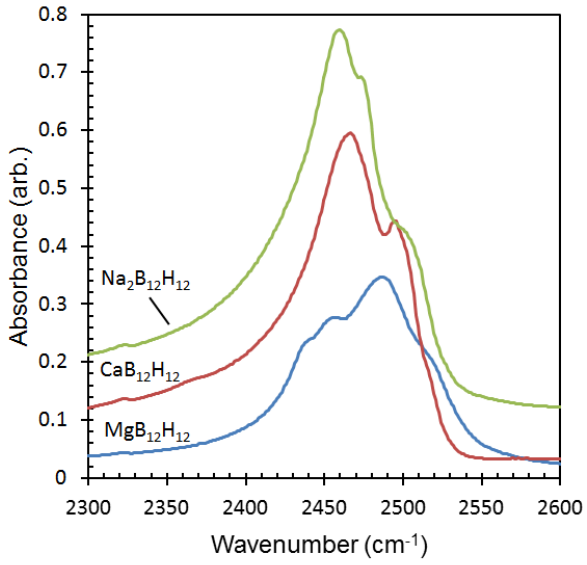

Figure S4: FTIR spectra for $MgB_{12}H_{12}$, $CaB_{12}H_{12}$, and $Na_2B_{12}H_{12}$. The $Na_2B_{12}H_{12}$ spectrum has been rigidly shifted vertically by 0.1 absorbance units for clarity of presentation.

We note here that both solid state (under 3.5 GPa pressure) B_2H_6 and gas phase B_2H_6 have a very strong vibrational B-H stretches from 2500 – 2600 cm^{-1}.[6] As indicated by Figure 2(b) there is no sign of peaks in this region where the B-H stretch of B_2H_6 would be found. Thus trapped intermediates similar to B_2H_6 can be excluded from the intial hydrogenation of MgB_2.

We performed an analysis assessing the level of sensitivity of the FTIR to suspected intermediates. Figure S5 shows a vertically expanded plot of the FTIR spectrum of MgB_2 + 0.85 wt. % H. We also show in Figure S5 a composite spectrum made by multiplying the experimental FTIR spectrum of $MgB_{12}H_{12}$ by 1.0 % and adding it to the FTIR spectrum of MgB_2. This composite spectrum is meant to mimic a sample in which 1.0 % of the MgB_2 formula units have been hydrogenated to $MgB_{12}H_{12}$ as an intermediate.

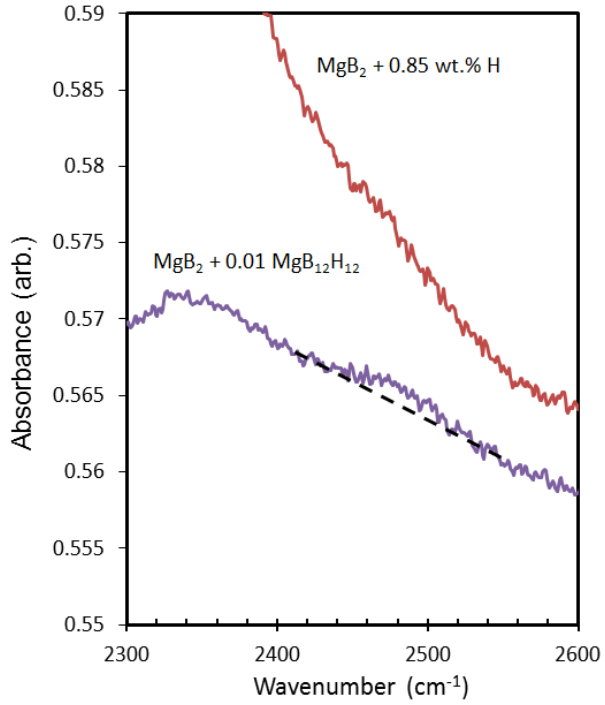

Figure S5: FTIR data for MgB_2 hydrogenated to 0.85 wt.% H compared to a composite spectrum consisting of MgB_2 + 0.01 $MgB_{12}H_{12}$. The MgB_2 + 0.85 wt.% H spectrum has been rigidly shifted vertically by 0.265 absorbance units for clarity of presentation.

The FTIR peak from $MgB_{12}H_{12}$ in the composite spectrum is highlighted underneath with a dashed line. As can be seen, the FTIR spectra are of sufficiently high statistics that if 1% of the MgB_2 sample were converted to $MgB_{12}H_{12}$, we would be able to detect it.

Figure S6 shows an expansion of the FTIR spectrum of MgB_2 + 0.85 wt. % H in the region 2300 – 2600 cm^{-1} in a search for $[B_3H_8]^-$ intermediates. We show in Figure S6 a composite spectrum made by multiplying the experimental FTIR spectrum of NaB_3H_8 by 1.0 % and adding it to the FTIR spectrum of MgB_2.

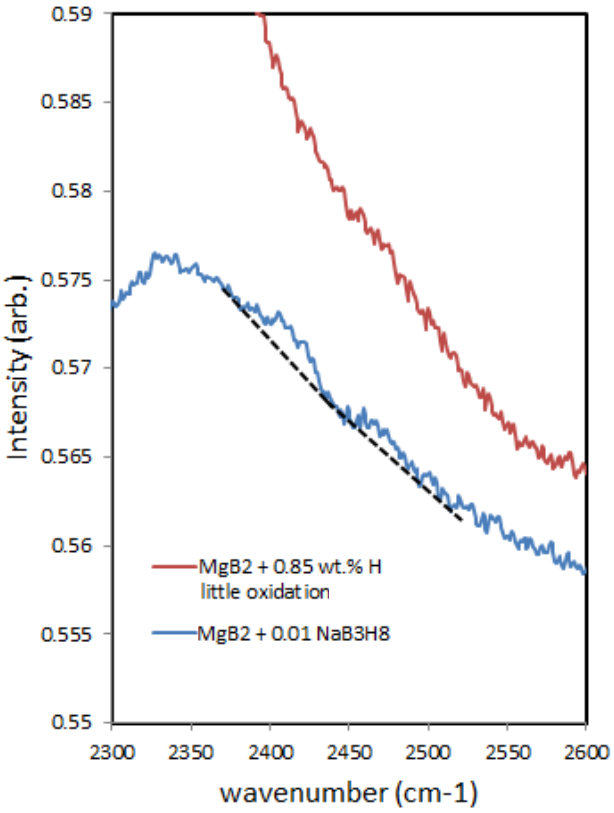

Figure S6: FTIR data for MgB_2 hydrogenated to 0.85 wt.% H compared to a composite spectrum consisting of MgB_2 + 0.01 NaB_3H_8. The MgB_2 + 0.85 wt.% H spectrum has been rigidly shifted vertically by 0.265 absorbance units for clarity of presentation.

This composite spectrum is meant to mimic a sample in which 1 % of the MgB_2 formula units have been hydrogenated to $Mg(B_3H_8)_2$. The FTIR peaks in the composite spectrum from $[B_3H_8]^-$ are highlighted underneath with a dashed line. As can be seen, the FTIR spectra are of sufficiently high statistics that if 1% of the sample were MgB_3H_8, we would be able to easily detect it.

By the analysis presented in Figures S5 and S6, we claim a FTIR detection sensitivity for intermediates to be 0.5 mol. % for the $MgB_2/Mg(BH_4)_2$ system.

Electronic structure analysis: To elucidate the differences in electronic structure between several boron containing materials, we plot the electronic density of states (DOS) for $MgB_{12}H_{12}$, $Mg(BH_4)_2$, and B_2O_3 in Figure S7, calculated with DFT. For more information and the DOS for MgB_2, see the discussion in Section 3.3 of the main text. We also include the calculated B K-edge XAS for MgB_2 intercalated with 0.85 wt. % H, compared to pristine MgB_2.

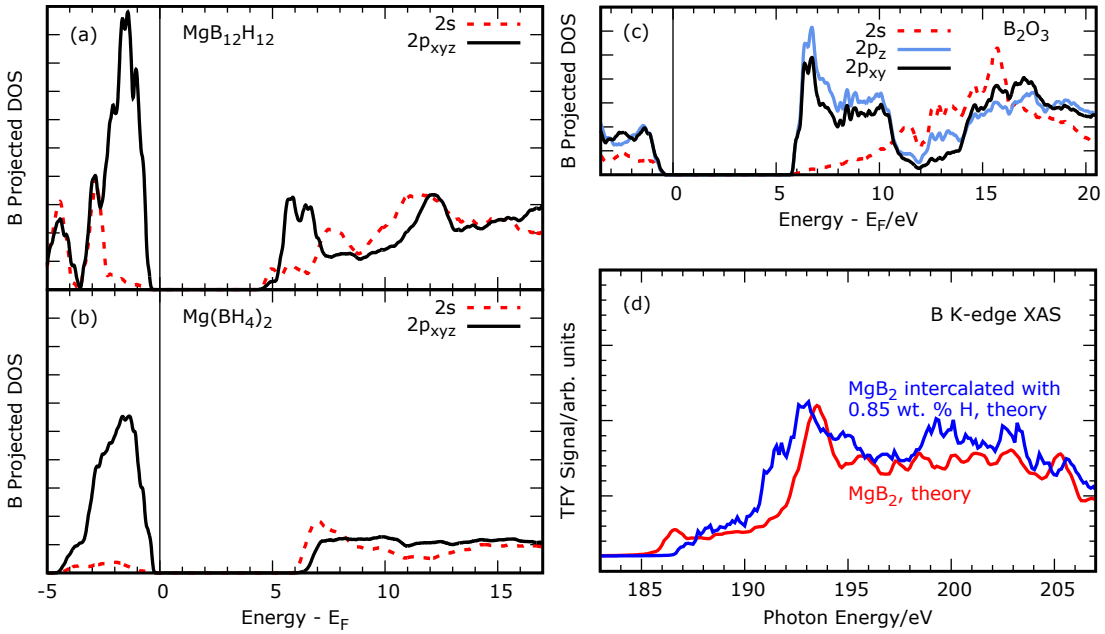

Figure S7: (a) $MgB_{12}H_{12}$, (b) $Mg(BH_4)_2$, and (c) B_2O_3 calculated orbital resolved DOS. (d) Calculated B K-edge XAS spectra for H-intercalated MgB_2 and for pristine MgB_2.

Kinetic modeling. To verify and systematically analyze the proposed hydrogenation mechanism, we have devised a kinetic model that combines relevant non-equilibrium chemical processes. In particular, the proposed mechanism involves successive chemical processes including H_2 molecule dissociation and adsorption of dissociated atomic H mediated by surface diffusion ("diffusive adsorption", hereafter) from the dissociation sites to the edge binding sites as the following:

$$H_2\ (g) \leftrightarrow 2H^* \leftrightarrow 2H_{ads}\ ,$$

where H^* indicates the intermediate state for adsorption at a reactive site and H_{ads} represents binding of hydrogen to the edges of hexagonal boron in MgB_2. Note that the first step represents the dissociation/association reactions of hydrogen at the reactive surface sites and the second step represents the diffusive adsorption/desorption of atomic hydrogen. We first constructed the energy diagram (Figure 9(b)) by accounting for the associated energetics obtained from our *ab initio* calculations and Arrhenius kinetic analysis for identifying the energy barriers of the corresponding chemical processes. For extracting the dissociation barrier, we considered the first kinetic regime (very initial

uptake) identified by our Arrhenius analysis. As shown in Figure S8, the average barrier is identified as E_{diss} (=0.914eV) within the full width at half maximum (FWHM) of the initial high barrier regime where the heterogeneous process occurs. On the other hand, to extract the diffusive adsorption barrier, we chose the second kinetic regime in Figure S8. By considering the regime exhibiting the high quality of the Arrhenius fits ($R^2 \geq 0.96$), we obtained E_{ads}=0.559eV as shown in the figure.

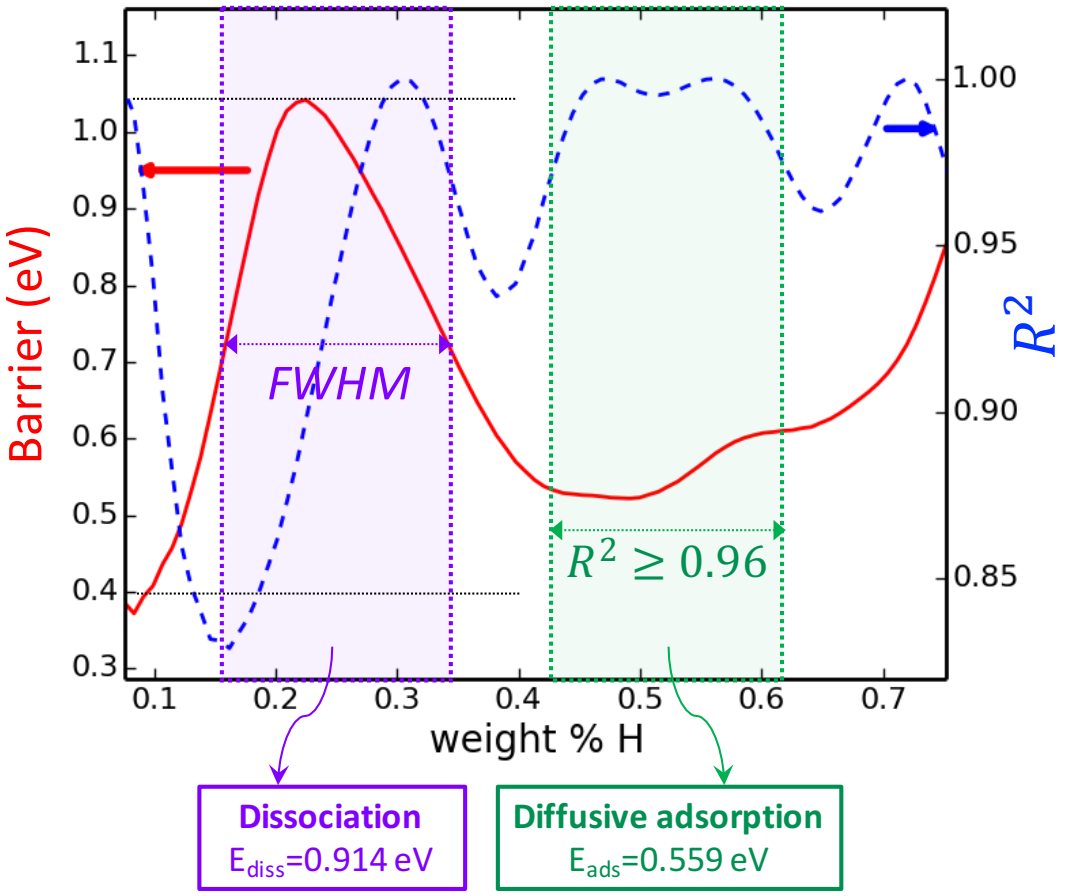

Figure S8: Arrhenius analysis for extracting the dissociation and adsorption energy barriers.

The energetics associated with the backward reactions (*i.e.*, association and desorption) incorporate the relevant binding energies as indicated in our energy diagram (see Figure 9(b)). The hydrogen binding energy at reactive MgB_2 basal planes (e_b^{Surf}) with respect to $H_2(g)$, which is associated with the association reaction, is given as $-0.202eV/H\ atom$ (note that we use $E_b^{surf} = 2|e_b^{Surf}|$ per 2H for our energy diagram) by the *ab initio* calculation. Therefore, the association barrier (E^{asso}) becomes $1.318eV$ ($=E_b^{Surf} + E^{diss}$). For the hydrogen binding energy at the eventual binding sites (edge sites) of MgB_2, which is necessary for the desorption barrier, we also employed the *ab initio* calculations.

Since the adsorbed hydrogen is accumulated at edge binding sites as hydrogenation proceeds, we considered the site coverage-dependent binding energies ($e_b^{Edge}(\theta)$). We first computed the average hydrogen binding energy per hydrogen atom for θ=1/15, 2/15, 5/15, 14/15, 15/15 by averaging the total energy variation over the total number of bound hydrogen atoms. These *ab initio* calculation results can be well fitted to the 4th order polynomial as shown in Figure S9(a). Informed by the polynomial fitting, we may extract the actual binding energy of an individual hydrogen atom participating in the binding event at the given site coverage. The extracted binding energy is also given as the 4th order polynomial as shown in Figure S9(b). Based on the binding energy, we may obtain the desorption energy barrier (E^{des}) as $E_b^{Edge}(\theta) - E_b^{Surf} + E^{ads} = 2 \cdot \left|e_b^{Edge}(\theta)\right| + 0.155$ (eV).

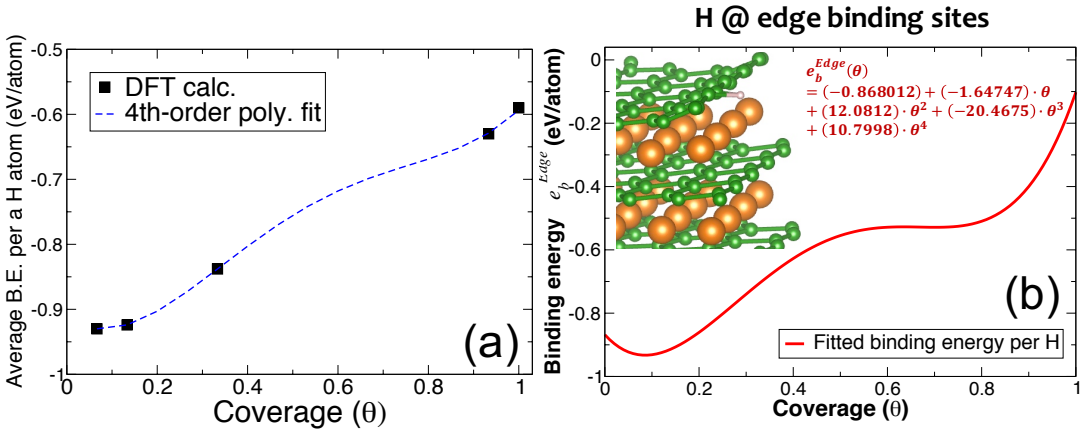

Figure S9: Site coverage-dependent hydrogen average, (a), and additional hydrogen, (b), binding energy at the edge binding sites computed by our *ab initio* calculations.

Using the constructed energy diagram, a simple reaction rate law, and a well-established isotherm model,[7] we carefully derived a mathematical model of reaction equations for the successive dissociation/association and diffusive adsorption/desorption processes as described in the *Method section* of the main text. The system of the differential equations is numerically solved simultaneously to capture the interactions between the two processes. Note again that this model contains some elements that are computed (*e.g.*, *ab initio* calculation-derived hydrogen binding energetics for different coverages), some that are measured (*e.g.*, experimentally derived activation energies), and some that are purely descriptive (*e.g.*, prefactors for the kinetic rate constants fitted to match simulated and experimental uptake curves). The associated computed and fitted values are tabulated in Table S1.

Table S1: Computed or fitted model parameters

Parameter	Value	Parameter	Value	Parameter	Value
k_1^0	1.286×10^4 $(wt.\% \cdot h^{-1} \cdot atm^{-1})$	E^{diss}	0.914 (eV)	$c_{ads,s}^0$	55.8 $(wt.\%)$
$\tilde{k}_1^0$	2.838×10^9 $(wt.\% \cdot h^{-1})$	E^{asso}	1.318 (eV)	c_s^0	49.4 $(wt.\%^{1/3})$
k_2^0	2.255×10^3 $(wt.\%^{-2} \cdot h^{-1})$	E^{ads}	0.559 (eV)	E^{acc}	0.222 (eV)
$\tilde{k}_2^0$	5.000×10^3 (h^{-1})	$E^{des}(\theta)$	$E_b^{Edge}(\theta) - E_b^{Surf} + E^{ads} = 2 \cdot \left\|e_b^{Edge}(\theta)\right\| + 0.155$ (eV)		

For controlled simulations with the manipulated rates of the operating reactions, we applied the additional multipliers f_{rate} to the kinetic coefficients (k_1, $\tilde{k}_1$, k_2, and $\tilde{k}_2$) in the governing differential equations as $k' = f_{rate} \cdot k$. By increasing f_{rate}, we may control the relative rates of individual reactions. For example, with an increasing magnitude of f_{rate} for k_1 (and $\tilde{k}_1$), we can simulate the hydrogen uptake kinetics more limited by the diffusive adsorption/desorption reaction. For the simulation results in the main text, we use f_{rate}=2000 to represent the reactions entirely controlled by one particular reaction step. Figure S10 includes the simulated behaviors of kinetic rate curves for the three experimental temperatures (364°C, 378°C, and 391°C). The information about the identified kinetic behaviors from our kinetic modeling and simulations is expected to be useful for analyzing the experimentally observed initial hydrogen uptake curves for different conditions.

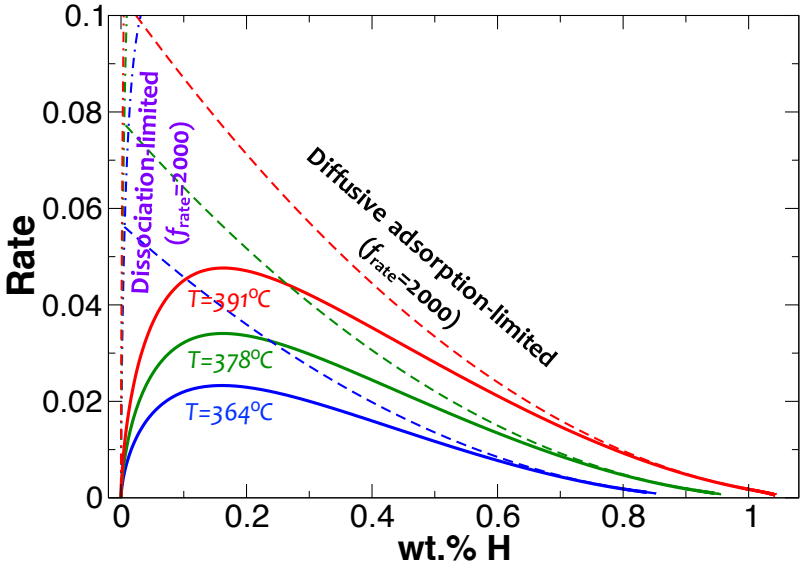

Figure S10: Simulated rate curves for the three experimental temperatures along with controlled reaction rates for f_{rate}=2000.

Dehydrogenation Sieverts mesasurement: We present in Figure S11 Sieverts results for the dehydrogenation of the partially hydrogenated MgB_2 sample.

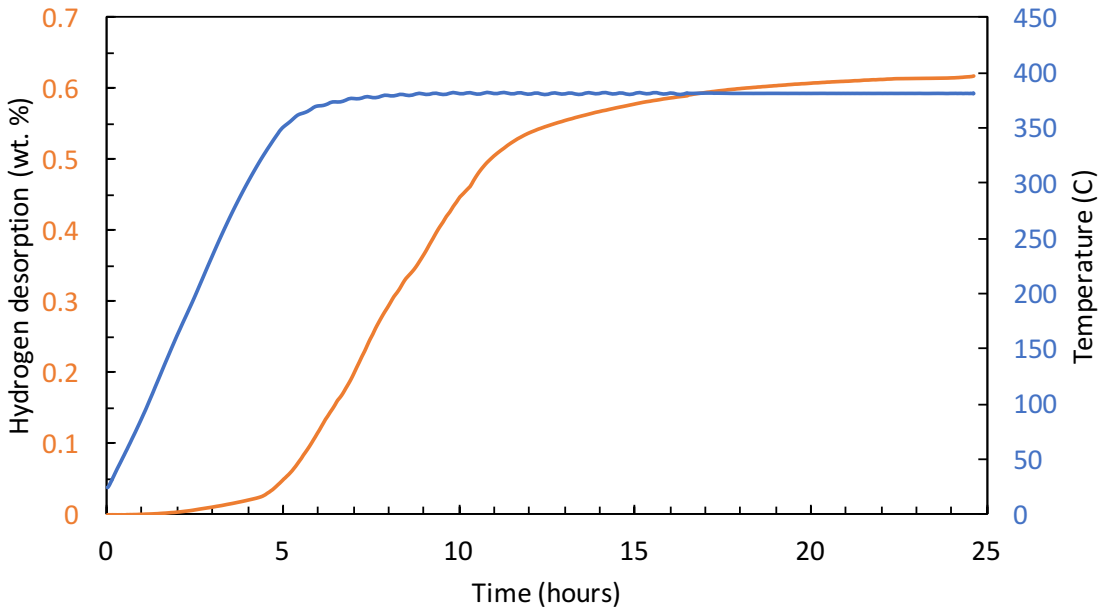

Figure S11: Hydrogen desorption for partially hydrogenated (0.85 wt. % H) MgB_2 in a Sieverts apparatus at a temperature of 381°C.

References

1 J. Stohr, NEXAFS Spectroscopy, Springer-Verlag, Berlin 2013.; J. A. Carlisle, E. L. Shirley, E. A. Hudson, L. J. Terminello, T. A. Callcott, J. J. Jia, D. L. Ederer, R. C. C. Perera, and F. J. Himpsel, Phys. Rev. Lett., 1995, **74**, 1234.

2 J. R. I. Lee, M. Bagge-Hansen, T. M. Willey, R. W. Meulenberg, M. H. Nielsen, I. C. Tran, and T. van Buuren, Research Methods in Biomineralization Science, 2013, **532**, 165.

3 A. Erbil, G.S. Cargill III, R. Frahm, and R.F Boehme, Phys. Rev. B, 1988, **37**, 2450.

4 X-ray transmission information was calculated via the website of the Center for X-ray Optics (CXRO) of the Lawrence Berkeley National Laboratory, http://henke.lbl.gov/optical_constants/filter2.html, accessed Dec 2016

5 Terry Udovic, private communication to L.E. Klebanoff, July 21 2016.

6 Y. Song, C. Murli, and Z. Liu, J. Chem. Phys., 2009, **131**, 174506.

7 P. W. Atkins, Physical Chemistry, 6th ed., Oxford University Press, Oxford 1998